

CAU-summer 2024

Khaled Hasan

supervised by: Johannes S. Martin, Prof. S. Wolf

August 2024

1 Introduction

Protoplanetary disks are rotating disks of gas and dust that surround newly formed stars. These disks eventually evolve into planetary systems, making the study of protoplanetary disks essential for understanding planet formation. Specifically, examining the chemical composition of these disks is crucial for predicting the future environments of the planets that will form. In this context, the presence of water ice is particularly interesting, as it can indicate the potential for a habitat that could support life.

In this project, we aim to simulate the appearance of a passively heated protoplanetary disk with a specified density distribution and using two different dust mixtures (one with water ice and one without). we compare the resulting images to develop a method for observing and distinguishing the presence and spatial distribution of water ice in protoplanetary disks. Due to the computational complexity of this task, Monte Carlo methods are used, implemented in POLARIS program (POLARized Radiation Simulator).

2 Theory

2.1 Radiative transfer (RT) equation

POLARIS's function is to solve the radiative transfer equation:

$$\frac{1}{c} \frac{\partial I_\nu}{\partial t} + \frac{\partial I_\nu}{\partial \ell} + (k_{\nu,\alpha} + k_{\nu,s}) \rho I_\nu = j_\nu \rho + \frac{k_{\nu,s}}{4\pi} \rho \int_\Omega I_\nu d\Omega \quad (1)$$

where I_ν is the spectral radiance at frequency ν (wavelength $\lambda = c/\nu$), j_ν is the emission coefficient, $k_{\nu,s}$ is the scattering opacity, $k_{\nu,a}$ is the absorption opacity, and ρ is the mass density. There is also a general form for the steady state case

($\frac{\partial I}{\partial t} = 0$), which includes polarization

$$\frac{d}{d\ell} \begin{pmatrix} I \\ Q \\ U \\ V \end{pmatrix} = - \begin{pmatrix} \alpha_I & \alpha_Q & \alpha_U & \alpha_V \\ \alpha_Q & \alpha_I & \kappa_V & \kappa_U \\ \alpha_U & -\kappa_V & \alpha_I & \kappa_Q \\ \alpha_V & -\kappa_U & -\kappa_Q & \alpha_I \end{pmatrix} \begin{pmatrix} I \\ Q \\ U \\ V \end{pmatrix} + \begin{pmatrix} j_I \\ j_Q \\ j_U \\ j_V \end{pmatrix} \quad (2)$$

$\{\kappa_i\}$ and $\{\alpha_i\}$ $I \in \{I, Q, U, V\}$ are extinction coefficients.

To solve the RT equation, POLARIS simulations of the protoplanetary disk are divided into 3 parts, temperature grid calculation, photon emission due to dust temperature, and scattering from the dust. Given a specific model consisting a grid, with specified dust mass density function and parameters related to the astronomical object like radii, distances, and positions. POLARIS calculates the temperature distribution and creates a new grid with additional temperature values for each cell, later, this temperature grid will be used to calculate the emissions and scattering.

2.2 Solving the RT equation

Using POLARIS, the solution to the RT equation is done on 3 phases, first the temperature grid is calculated, next, the dust emission simulations are performed using the temperature grid. Parallel to dust and temperature simulations the dust scattering simulation are performed. In this project, we were only interested in the intensity, therefore, we will be ignoring the components (Q , U and V in the Stokes vector).

2.2.1 Temperature simulations

Temperature simulations uses Monte Carlo Photon transfer to calculate the dust heating due to absorption and emission, first the emissivity is calculated for a range of temperatures assuming a spherical dust shape for simplicity. Then photon transfer is performed, where for each photon package carrying energy ϵ that passes through a cell with path length ℓ the energy per unit time in the cell is incremented (absorbed) by

$$\dot{E} = \frac{\epsilon}{V_{\text{cell}} \Delta t} C_{\text{abs}, \lambda_i} \ell \quad (3)$$

where \dot{E} is the stored energy per unit time V_{cell} is the volume of the cell, $\epsilon/\Delta t$ is the photon initial energy per time, $C_{\text{abs}, \lambda_i}$ is the dust cross section of absorption and ℓ_i is the path through the cell.

After the contribution from all photons is included, it is compared to an interpolated emissivities and the temperature for the required cell is calculated. The detailed algorithm was described by Bjorkman and Wood in [2].

2.2.2 Dust emission simulations

After the temperature grid is made, the dust emission simulations are performed. Ignoring the scattering terms in equation 1 these simulations provide the first order solution to the RT equation. This is done by using ray-tracing (without using Monte Carlo simulations). The emissivity of each cell is calculated using the temperature grid and assuming a modified Blackbody radiation from each cell with a given temperature. Each cell is a photon package source emitting photons with Energy

$$\dot{E}_\lambda = \frac{4\pi}{N_{\text{ph}}} \sum_{\text{cells}} N_d C_{\text{abs},\lambda} B_\lambda(T_d) \quad (4)$$

where B_λ is the Planck radiation law function, T_d is the dust temperature, N_d is the number of dust grains in the cell and N_{ph} is the number of photon packages. Since this part uses integration rather than Monte Carlo it is faster than the scattering and temperature simulations.

In dust simulations, we added a background, the background is a constant emitting object with a given temperature, and a radiation given by

$$I = f B_\lambda(T_{\text{eff}}) \quad (5)$$

where f is a scaling factor, T_{eff} is the effective background temperature.

2.2.3 Dust scattering simulation

Using Monte Carlo techniques to solve the scattering part of equation 2 and the surface integral term of any external intensities arriving at the detector (integral term in 1), multiple photons will be emitted from source in random directions. A random number will be chosen from 0 to 1 (which will define the Monte Carlo steps) according to the distribution $\tau_{st} = -\ln(1 - z)$, $z \in [0, 1)$, then accumulating the optical depth of extinction such that it is always smaller than τ_{st} (if it got bigger in some cell, it won't interact with that cell) after interacting with each cell, the photons are re-emitted at a different angle and wavelength.

2.3 Disk model

2.3.1 Grid

The grid is the space where the RT equation is to be solved. Since we are dealing with real space, 3D grids are being used, these grids can be divided based on what coordinates they are using. POLARIS provides 4 different geometries including spherical and cylindrical grids, in our case we used cylindrical grid in all simulations.

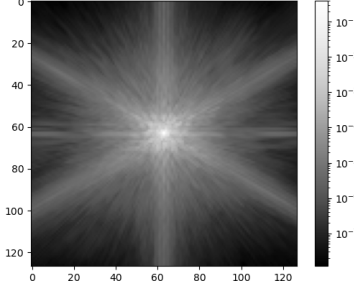


Figure 1: Example of a point spread function calculated for James Webb NIRcam F070W filter using python's webbpsf library

2.3.2 Disk density function

Following the model presented in [3]. The disk density function is given by

$$\rho(r, z) \propto \left(\frac{r}{R_{\text{ref}}}\right)^{-\alpha} \exp\left[-\left(\frac{r}{R_{\text{outer, grid}}}\right)^{2-\gamma}\right] \exp\left[-\frac{1}{2}\left(\frac{z}{h_g(r)}\right)^2\right] \quad (6)$$

Where h_g is the scale height and is given by $h_g(r) = h_{\text{ref}}(r/R_{\text{ref}})^\beta$, the proportionality constant is then obtained by normalization.

2.4 Point spread function

Observed images by telescopes look different from that of modeled theoretically as the image will be subject to spreading (blurring) and other distortions from the mirrors. Therefor, in order to retrieve observed images we shall convolve them with the Point Spread Function (PSF).

PSF is a 2D kernel that depicts the optical response of a point source. By convolving this kernel over the whole image, we get the response of the whole input image. In this project, as we were concerned with Jame Webb images, we obtained the PSFs for the different James Webb NIRcam filters from the [webbpsf python library](#) that calculates the PSF for different filters with different wavelength ranges.

3 Numerical methods

3.1 POLARIS files

3.1.1 temp

Temperature simulation, will take in a grid, a photon source and dust components. After the simulation, a new grid will be formed, which has additional

physical quantity "Temperature" assigned to each cell, the temperature will be added at the positions denoted by index $ID_{\text{phys}} = \{2, 3\}$, for dust and gas temperatures respectively, in the grid file. For our simulations, we assume both temperatures are equal.

3.1.2 dust files

In dust files we input a temperature grid and dust components, and detectors. The results are 6 emission images for to each defined detector, representing (I, U, Q, V) , optical depth and column density.

To add a background to the dust simulations, the following command should be used:

```
<source.background nr_photons = "N_ph" > f [a.u.] T_eff q u v alpha_1 alpha_2
```

finding T_{eff} and f is not trivial, a paper on the structure of Orion Nebula [1] reports the values 10 000 K, which was first used in our simulations. However, it was later changed to provide better observations for the stellar's shadow.

3.1.3 dust_mc files

These files represent the scattering simulation code. Where we define photon sources (Star, and dust in case of self scattering), a detector (almost similar to that for the dust simulation 3.1.2, but without a background ID parameter), a grid and dust mixtures.

3.2 Grid

To define a grid in POLARIS, the polaris-gen command is used, for the detailed usage, refer to the [github documentary of POLARIS](#) [5].

After the generation of the grid, a binary (.dat) file is generated at `./POLARIS/$MODEL_NAME(custom_disk my case)/` the resulting grid will not include the temperatures of the cells, therefore, after the temperature simulation, a new modified grid is produced and is called `grid_temp.dat`, this file will have additional column with $ID = 2$ and 3 to store dust and gas temperatures.

In simulations with more than one dust mixture (like water ice for example) one should add an additional column with $ID = 21$ where each cell will be given a mixture id ID_{mix} .

3.3 Density

By comparing with the equation 6 with that from [3] we find a difference in the variables definition, where $\gamma = \alpha - \beta$. In the default implementation in

the grid model (`/POLARIS/tools/polaris_tools_modules/math.py`) the density will cut off suddenly after $r = R_{\text{outer}}$, however, we changed it so that it will cut off after $r = R_{\text{outer, grid}}$. The original default disk density function was implemented so that R_{out} is the cutoff radius, we added a parameter called `"real_outer_radius"` so that after this radius the density will start the exponential vanishing until it reaches `"outer_radius"`.

3.4 Model parameters

As we are investigating protoplanetary disk, we chose to run simulations on the d216-0939 object, which would due to its orientation allow us to observe absorption and get a clear idea of the spatial distribution of water ice. The star in the middle of the stellar is 362 pc away from earth, has same luminosity as the sun, with temperature $T_{\text{star}} = 4140$ K therefore following from the luminosity formula

$$L = 4\pi\sigma R^2 T^4 \quad (7)$$

then the radius of the star is $R_{\text{star}} = 1.944R_{\odot}$.

The grid used is a custom disk (custom since we changed the function) cylindrical grid with $R_{\text{min}} = 0.05\text{AU}$, $R_{\text{out}} = 300\text{AU}$, and for the grid edges $R_{\text{outer, grid}} = Z_{\text{max}} = 1000\text{AU}$. The gas mass is $4 \times 10^{-4}M_{\odot}$ and the dust ratio is 1/100 of the gas. R_{ref} and h_{ref} are 100AU and 15AU respectively. α and β are 1.875 and 1.125. Last, N_r is 100 (Default) for most simulations and $f_r = 1.03$ (Default). As a result, the radial cell distribution followed an exponential form, where:

$$r_i = R_{\text{min}} + \frac{f_r^i - 1}{f_r^{N_r} - 1} (R_{\text{outer, grid}} - R_{\text{min}}) \quad (8)$$

The detectors are all at distance 362 pc and 72.5° inclination unless otherwise specified.

We will refer to d216-0939 object as a young stellar object (YSO)

4 Results

4.1 Images of a Young Stellar Object

First, to test the codes, we tried to reproduce previous results from Johannes Martin's work, where he considered the young stellar object discussed in 3.4 using many wavelengths including $\{0.656\mu\text{m}, 1.6\mu\text{m}, 2.8\mu\text{m}\}$. The pre-convolved images are shown in Figure 2 which matched his results. However, after convolving with the PSFs associated with F070W, F162M, and F277W filters respectively, the results plotted in Figure 3 shows that for longer wavelengths, the YSO structure is no longer apparent, and it is dominated by the star resulting in a one point source.

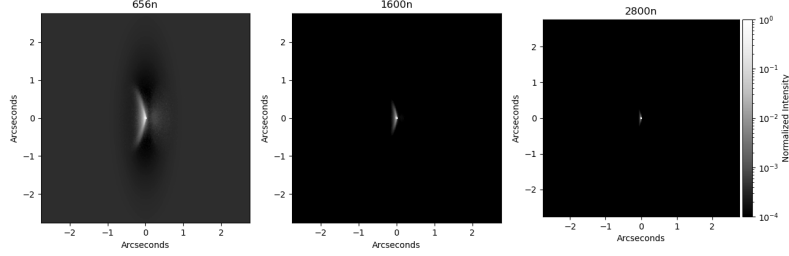


Figure 2: Non-convolved images of the young stellar object described above

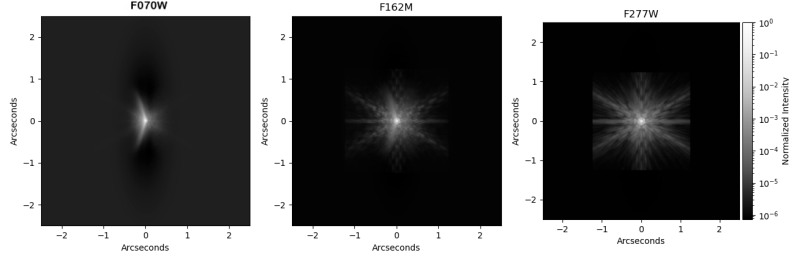


Figure 3: Convolved images of the young stellar object

As a result, due to the higher intensity for the higher wavelengths, the composite images do not show structure as they are dominated by higher wavelengths.

4.2 Background temperature selection

The intensity of the background is given by $I = f B_\lambda(T)$ where $B_\lambda(T)$ is given by:

$$B_\lambda(T) = \frac{2hc^2}{\lambda^5} \frac{1}{\exp(ch/(\lambda k_B T)) - 1} \quad (9)$$

As shown in Figure 5, for high temperatures, the emitted energy has a sharp peak at specific critical wavelengths, while decaying as the wavelength changes meaning. As a result the background will be insignificant for wavelengths far from the critical value.

A proposed solution to this problem is to decrease the temperature as much as possible, while at the same time increasing the scale factor f so that the intensity flattens and becomes comparable at different wavelengths. Then the

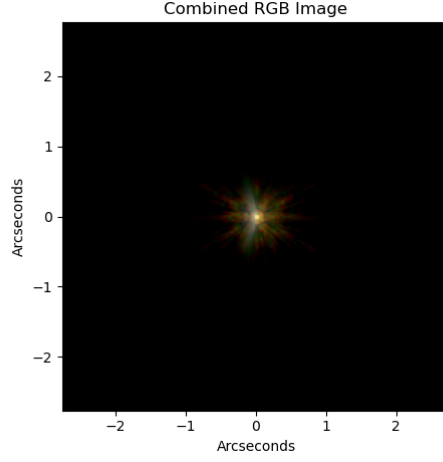


Figure 4: Colored rgb image of combined ($r : 2.8\mu\text{m}, g : 1.6\mu\text{m}, b : 0.656\mu\text{m}$) images and $v_{\text{min}} = 10^{-5}$. Towards the center of the combined image a white "bow" is visible due to contribution where the intensity is highest

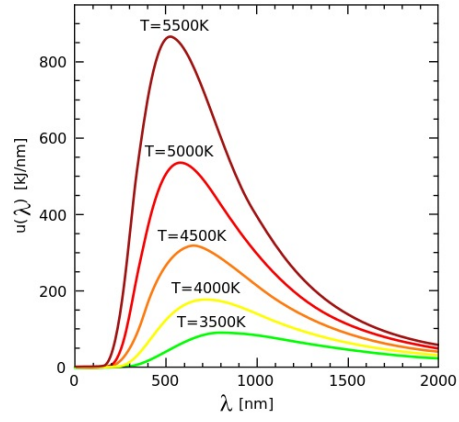


Figure 5: Radiation Energy density per wavelength at different temperatures, $B_\lambda(T) = c/4\pi u_T(\lambda)$. [4]

shadow of d216-0939 should be visible. In order to obtain the suitable value for the scale factor for as low temperatures as 1000 K, we ran the simulations for different orders, we considered the intensity of the background for the test case ($T = 10\,000$ K and $f = 1.5 \times 10^{-15}$) and considered a background with similar intensity at $1.6\mu\text{m}$ using equation 5, subsequently we changed the temperature to 1000 K and tested different orders for scale factors, note that due to the logarithmic scale of the optical properties of the images, we only need to search for the right order that will lead to a visible shadow.

And by convolving based on the wavelength filter, the following figure is obtained

Based on figures 6 and 7, the chosen scaling factor for the 1000 K was $f = 1.31 \times 10^{-08}$. All proceeding results will use this background unless otherwise mentioned.

4.3 Water ice

The water-ice properties (absorption of light) are expected to appear for wavelengths within the range $[2.5 - 4.4]\mu\text{m}$ and have a peak around $3.1\mu\text{m}$ (see Figure 9)[6]. In Figure 8, the difference between two simulations (with water ice - without water ice) is plotted for different wavelengths on a semi-log scale. Note that for the three figures around $3.1\mu\text{m}$ were dominated by blue color (Indicating photon absorption by water ice), which extends through the whole structure. While for wavelengths towards the edge of the water ice feature ($\lambda \in \{2.8, 4.1\}\mu\text{m}$) the water ice absorption is apparent towards the outer parts of the YSO. And for longer wavelengths the lower silicate ratio in the outer (lower temperature) regions, leads to lower absorption for the higher wavelengths and thus higher intensity for the water ice mixture.

In RGB image, the water ice spatial presence was slightly visible towards the outer parts of the disk. As in Figure 10. Here, green color was associated with the $3.1\mu\text{m}$ where we expect to see most water-ice features, and it is indeed notable that there were few scattered green spots far from the center of the disk, and we expect to see more with higher photons number.

4.4 High resolution circular mirror

James Webb's Mirrors are hexagonal with approximate diameter of approximately 6.5m, have we assumed a bigger mirror with a diameter of 12m and a circular shape, such that a Gaussian PSF will be sufficient. For the sake of comparison with results from subsection 4.1 the same background is going to be used ($f = 1.5 \times 10^{-13}$, $T = 10\,000$ K). The simulations resulted in the proceeding images.

comparing the colored figures might provide a nice insight on the what the picture from James Webb will look like compared to that of the proposed telescope.

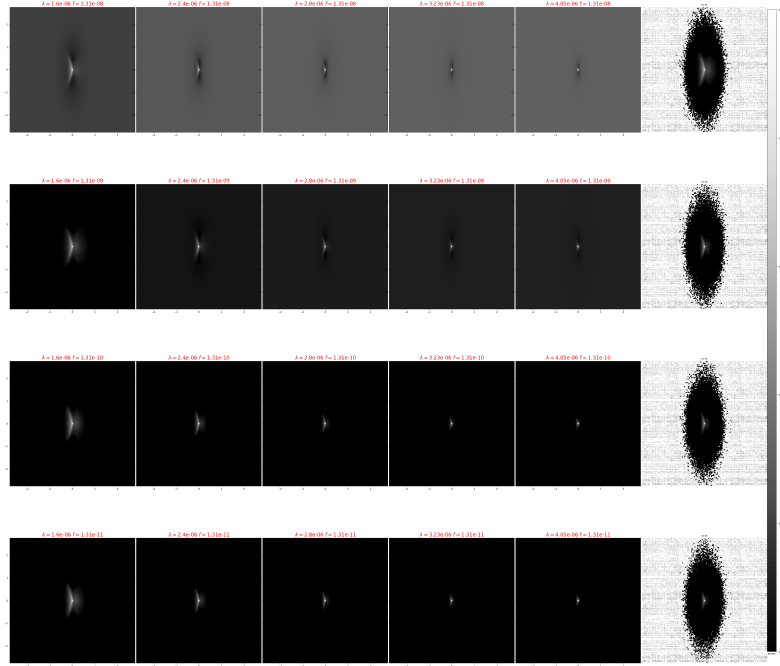


Figure 6: The plotted images of the YSO at different scaling factors and wavelengths for $T = 1000$ K, the label for each figure is printed on top of it. The last column on the right represent the No-Background case in ascending wavelength order for comparison purposes

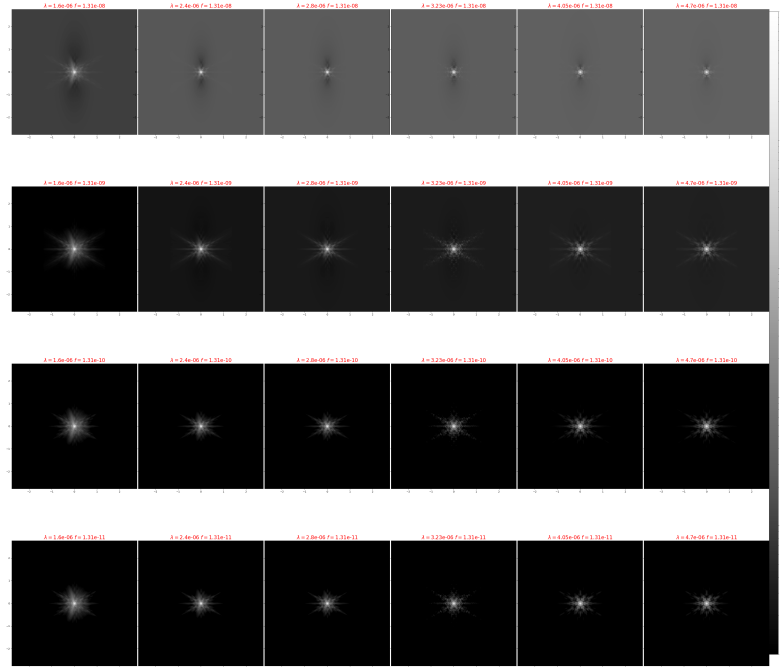


Figure 7: Convolved images from Figure 6 with appropriate kernel based on the wavelength

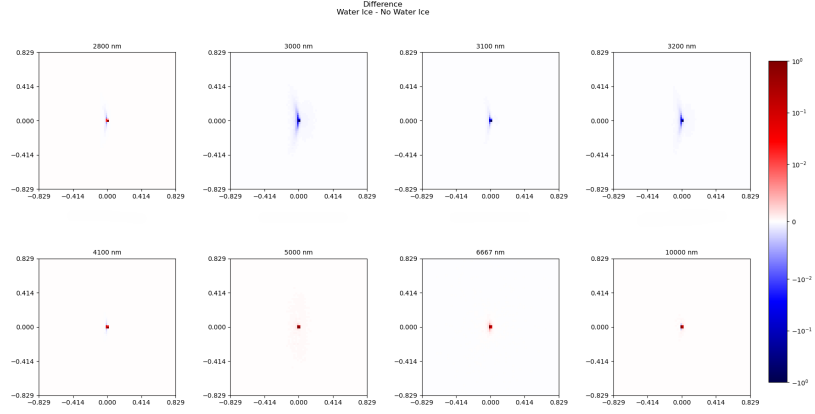


Figure 8: Images of the intensity difference between water ice simulations and simulations ran without a water ice mixture at different wavelengths. Axes are given in arc-seconds

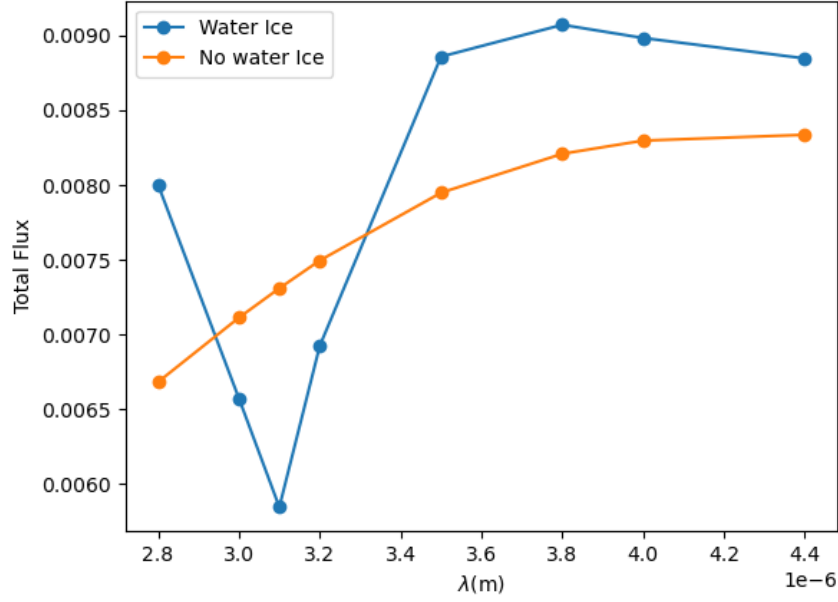


Figure 9: Calculated total flux of the scattered radiation vs. wavelength within the water ice feature. Note the dip at 3.1 μm

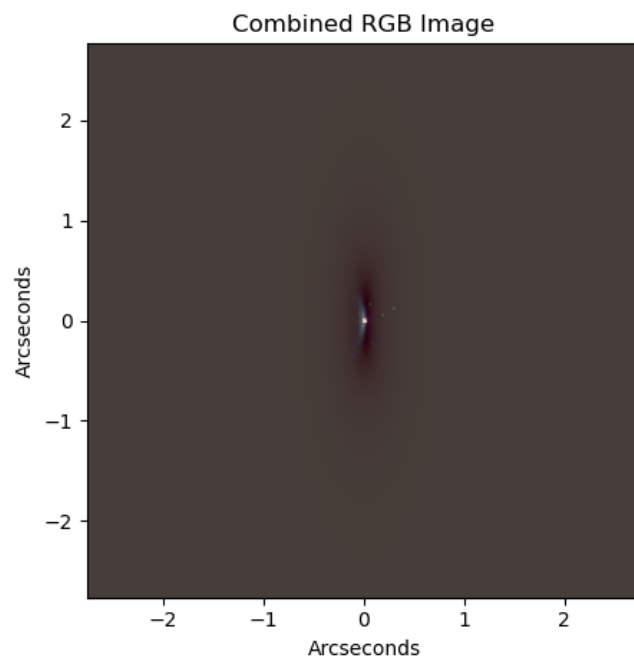


Figure 10: RGB combined image, r: $4\mu\text{m}$, g: $3.1\mu\text{m}$, b: $2.8\mu\text{m}$

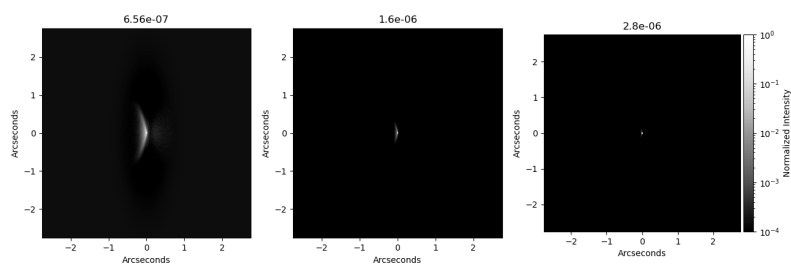


Figure 11: Images 2 reproduced with higher resolution mirror

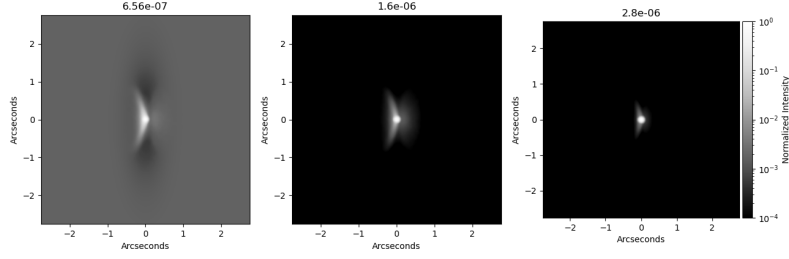
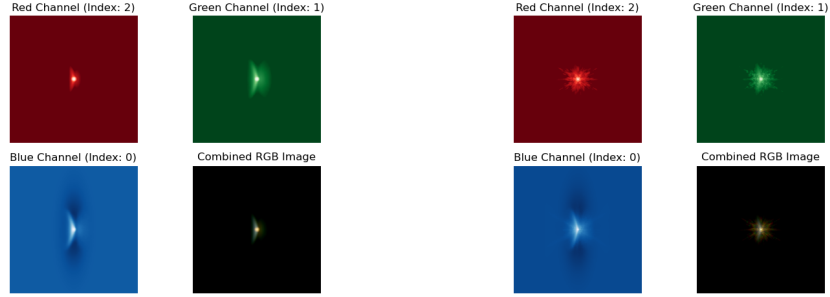


Figure 12: Images 12 convolved with the Gaussian PSF



(a) Image for the proposed telescope with a large mirror.

(b) Image for the James Webb Space Telescope.

Figure 13: Comparison of colored images between the proposed telescope with a large mirror (left) and the James Webb Space Telescope (right). The used wavelengths are: $[0.656, 1.6, 2.8]\mu\text{m}$ for blue, green and red respectively

4.5 Finer grid

As the radial cells distribution is exponential, having too few cells will risk losing a critical region in the grid that is closer to the star, for example, for as small values of N_r as 100, $r_1 = 1.7$ AU, while for larger values like $N_r = 250$ $r_1 = 0.069$ AU. Which lead to a very low maximum temperature in the first cases (around 270 K max) compared to the case of $N_r = 250$ radial points, where the maximum temperature went as high as 1300 K. This big difference is due to how far the cells get for small N_r values. Figure 14 depicts the temperature distributions for both grids. Despite the big difference in the temperature distributions, it only affects the inner parts of the YSO. In the normalized images this results in a dimmer background, as the maximum intensity from dust emission increases in the inner parts of the grid.

4.6 spatial distribution of water ice features

Motivated by results shown in Figure 10, we aim to investigate the spatial distribution of the water ice absorption. As water ice is present on the outer rim of the disk, the absorption starts to appear towards outer parts, then at wavelengths close to $3.1\mu\text{m}$ the features are stronger and the absorption is more apparent in the center, Figure 8.

By having a look at the emitted light, we can gain a perspective over what is being absorbed by water ice, Since we have a similar background, the background impact will not be visible apart from where water ice absorbs light. Figure 16a shows the normalized difference between water ice and no water ice dust emissions for 65° inclination. As the dust simulations performed by integration the figures are almost continuous and smooth. We can clearly see with smaller wavelengths in the water ice feature that the water ice is distributed on the outer regions, as well as in inner regions shaded by dust. For higher wavelengths closer to the water ice feature the absorption from water ice dominates the increase in emission that results from lower silicate ratio in the outer rim. Before the absorption contribution diminishes with the wavelength increase.

For higher inclination angles (lower edge-on inclinations). The distinctions made for the inner parts are no longer visible in the emission plots. Figure 16b.

With the dust scattering simulations, the difference in the scattered light is smaller for the outer regions (only appeared at small orders 10^{-4}). The scattering is remarkably significant at 72.5° Figure 17

5 Conclusion

From the results we obtain we can conclude the following:

1. James Webb telescope can sufficiently distinguish the YSO (d216-0939) at short wavelengths with the literature proposed background. Should the

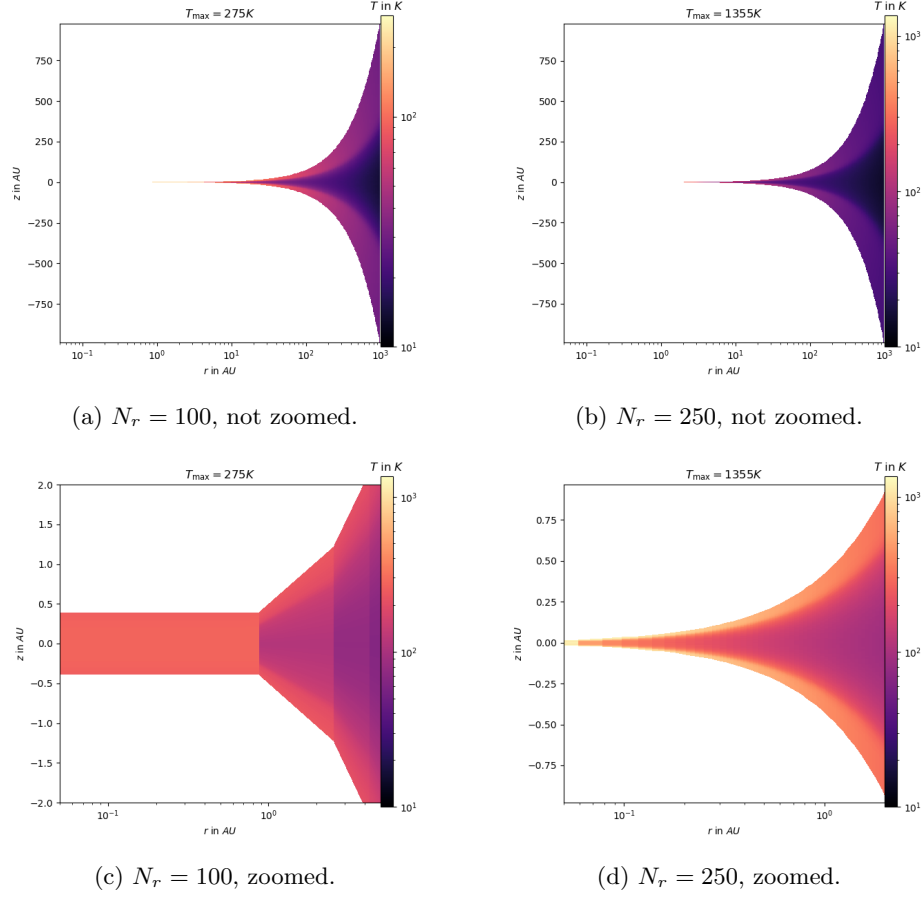


Figure 14: Temperature distributions for different radial grid sizes. The top row shows the non-zoomed images, while the bottom row shows the zoomed-in images.

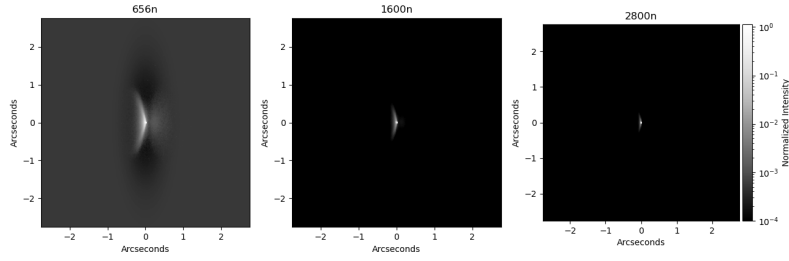
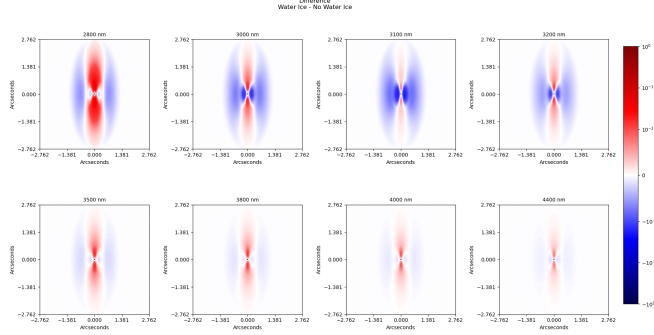
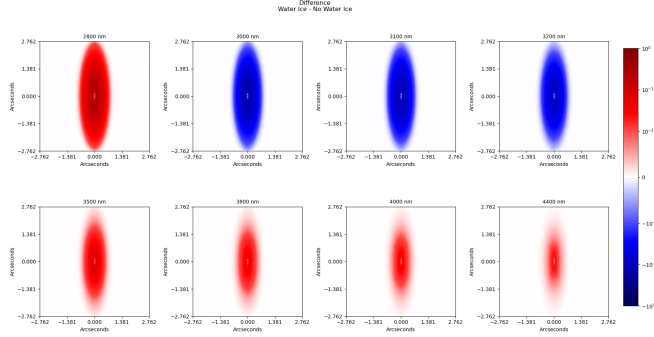


Figure 15: Reproduced results from 2 with finer grid $N_r = 250$ with max temperature $T_{\max} = 1355$ K



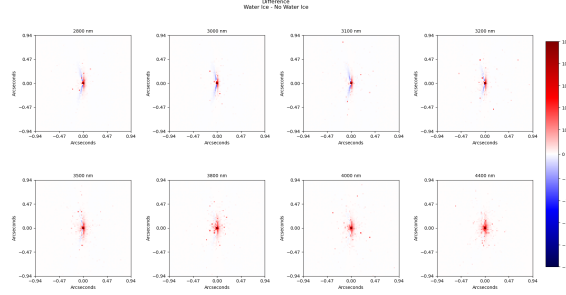
(a) Normalized difference between water ice and no water ice dust emissions for 65° inclination.



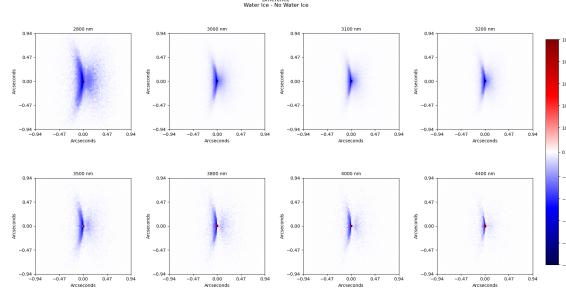
(b) Normalized difference between water ice and no water ice dust emissions for 75° inclination.

background changes it is possible to observe the stellar's shadow at higher wavelengths, but the structure remains vague.

2. The appearance of shadows at certain wavelengths imposes a constraint on the background temperature, for as high of temperatures as 10000 the shadow is visible up to $0.656\mu\text{m}$. While for low temperatures $\mathcal{O}(1000)$ the shadow could be observed up to $4\mu\text{m}$
3. Water ice features appear significantly as rise in absorption around the $3.1\mu\text{m}$ wavelengths. They can also be spatially distinguished as scattered spots on the outer rim of the disk.
4. Having a finer grid is necessary to accurately resolve temperature, and can provide clearer images for high wavelengths.
5. Choosing bigger circular mirror had the effect of a higher resolution images with more visible features at higher wavelengths after convolving with Gaussian PSF.



(a) Normalized difference between water ice and no water ice dust scattering for 65° inclination.



(b) Normalized difference between water ice and no water ice dust scattering for 72.5° inclination.

Figure 17: Comparison of normalized differences between water ice and no water ice dust scattering for 65° and 72.5° inclinations.

References

- [1] B. Balick, R. H. Gammon, and R. M. Hjellming. “The Structure of the Orion Nebula”. In: 86.513 (Oct. 1974), p. 616. DOI: [10.1086/129654](https://doi.org/10.1086/129654).
- [2] J. E. Bjorkman and Kenneth Wood. “Radiative Equilibrium and Temperature Correction in Monte Carlo Radiation Transfer”. In: *The Astrophysical Journal* 554.1 (June 2001), pp. 615–623. ISSN: 1538-4357. DOI: [10.1086/321336](https://doi.org/10.1086/321336). URL: <http://dx.doi.org/10.1086/321336>.
- [3] K-H Hofmann et al. “VLTI-MATISSE L-and N-band aperture-synthesis imaging of the unclassified B [e] star FS Canis Majoris”. In: *Astronomy & Astrophysics* 658 (2022), A81.
- [4] Mini Physics. *Planck Radiation Law and Wien’s Displacement Law*. <https://www.miniphysics.com/uy1-planck-radiation-law-and-wien.html>. Accessed: 2024-08-15. n.d.

- [5] *POLARIS Quickstart*. github.com/polaris-MCRT/POLARIS/blob/master-basic/QUICKSTART.md.
- [6] Hiroshi Terada and Alan T. Tokunaga. “Discovery of Crystallized Water Ice in a Silhouette Disk in the M43 Region”. In: 753.1, 19 (July 2012), p. 19. DOI: [10.1088/0004-637X/753/1/19](https://doi.org/10.1088/0004-637X/753/1/19). arXiv: [1204.5503](https://arxiv.org/abs/1204.5503) [[astro-ph.EP](#)].